

## **IMPLICATION OF RUPTURE PROCESS AND SITE EFFECTS IN THE SPATIAL DISTRIBUTION AND AMPLITUDE OF THE NEAR-FAULT GROUND MOTION FROM THE 2004 PARKFIELD EARTHQUAKE**

Arben Pitarka, Nancy Collins, Hong-Kie Thio, Robert Graves and Paul Somerville

URS Corporation, Pasadena, California

### **Abstract**

The 2004  $M_w$ 6 Parkfield earthquake is the last in a series of several strike-slip earthquakes that have occurred on the same fault located in a zone that marks the transition between a creeping section and a locked section of the San Andreas Fault in central California. Ground motion data recorded at a dense network of near-fault stations installed by California Geological Survey (CGC) and United States Geological Survey (USGS) are unprecedented in terms of quality and characteristics for this type of earthquake in California. Although of moderate size, the earthquake produced near-fault ground motion acceleration that exceeds predictions from empirical ground motion models. At three sites the recorded acceleration was more than 1.0g (Shakal et al., 2005). Very large peak ground velocities of up to 83cm/s were also recorded at both ends of the fault. On the other hand, most of the stations located very near to the fault recorded ground motion with very low acceleration and velocity. In this study we investigate the implication of the rupture kinematics and dynamics, and local site effects in the amplitude and spatial variation of the near-fault ground motion for this earthquake.

### **Near-Fault Ground Motion Characteristics**

Figure 1 shows the map of the Parkfield area and location of 47 CGC and 11 USGS strong motion recording stations used in this study. The Parkfield earthquake occurred on a right lateral segment of the San Andreas fault. The San Andreas fault forms the boundary between the granitic Salinian block on the west and Southern Diablo Range with sedimentary Franciscan terrane on the east (Dickinson 1966). Based on the distribution of aftershocks that occurred immediately after the earthquake the fault length and width were estimated to be 35km and 15 km, respectively (Hardebeck and Michael, 2004). No co-seismic surface rupture appeared, but surface slip began several hours after the main shock (Langbein et al., 2005). The fault plane has a strike angle of  $157^\circ$  and a dip angle of  $89^\circ$ . The shallow underground structure is characterized by the velocity contrast across the fault, with the northeast side about 20% slower in the top 10 km. Below 10 km the velocity contrast gradually diminishes with depth. Most of the strong motion sites are category B using NEHRP classification.

Figure 2 displays the fault-normal component of two selected acceleration time histories recorded at stations PF14 and PF15 located near the northern end of the fault. Their respective spectrograms are shown in figure 3. Station PF14 is located very close to the fault with a fault distance less than 1 km. The 1.3 g ground motion acceleration at this station is the highest peak acceleration recorded during the Parkfield earthquake (Shakal et al., 2005). Station PF15 is



located close to station PF14. The distance between the two stations is less than 3.5 km. The differences among the main features of the ground motion at these two stations are a clear illustration of the very complex near-fault ground motion. The acceleration at station PF14 is dominated by two source related large pulses, and a very short time duration. The pulses are energetic at a very narrow frequency band between 1Hz and 3Hz. In contrast, the acceleration time history at station PF15 has a much smaller amplitude and longer duration. Most energetic phases at this station have different arrival times and distinct frequency contents that are centered at 1Hz, 2.5 Hz. and 5Hz, respectively. Coda waves are mainly small amplitude pulses with a 1 sec period. Such striking dissimilarities between neighboring stations are also observed at other regions near the fault trace. They are indicative of fault zone effects that mainly suppress the high frequency signals of the ground motion while increasing its duration.

The comparison between the recorded peak acceleration and that predicted by the empirical attenuation model of Abrahamson and Silva (1997), for both fault-normal and fault-parallel components shown in Figures 3a and 3b, indicates that the stations that recorded ground motion below the expected value are all located within less than 1 km from the fault. In contrast, stations with higher than expected acceleration are clustered at fault distances between 2-4 km. At longer distances the recorded ground motion is slightly smaller than that predicted by the attenuation model at all analyzed frequencies. The generally low-level ground motion can be explained by the fact that this was a low stress drop event. The difference between fault-normal and fault-parallel components remains significant up to at least 3.3Hz. This is an interesting observation. It indicates that the rupture directivity for strike-slip event remains effective even at high frequencies.

These general observations indicate that the wide-spread differentiated near-fault motion may have been caused mainly by fault zone effects and local site effects. As it will be shown below, our study does not rule out the possibility of increased ground motion in some small areas near the north end of the fault where our rupture dynamics model shows small patches of larger stress-drop. Studies of fault-zone trapped waves have delineated a 150 m-wide fault zone characterized by low velocity and cracked rock (Li et al., 2006; Thurber et al., 2003). The width of the fault zone and that of damaged rock may vary along the fault. The fault zone weakens the high-frequency motion generated at the crack tip while amplifying trapped waves propagating along the fault. As a direct consequence, the scattered waves generated inside this zone, dominate the ground motion at near fault stations where the relatively low amplitude coda waves increase the ground motion duration significantly.

### Local Site Effects

We used the recorded motion from the 1983  $M_w$ 6.5 Coalinga earthquake to estimate the elastic local site response at Parkfield array stations that recorded both earthquakes. The stations used in analyses of local site effects are shown in Figure 4. The Coalinga earthquake occurred about 30 km NE of the epicenter of the Parkfield earthquake (Eberhart-Phillips, 1989). Given its large epicentral distance from the array, we assumed that the incoming motion from the Coalinga earthquake was the same at all Parkfield stations. The site effect was calculated as the ratio between the smoothed amplitude spectrum of recorded motion at each station and the reference

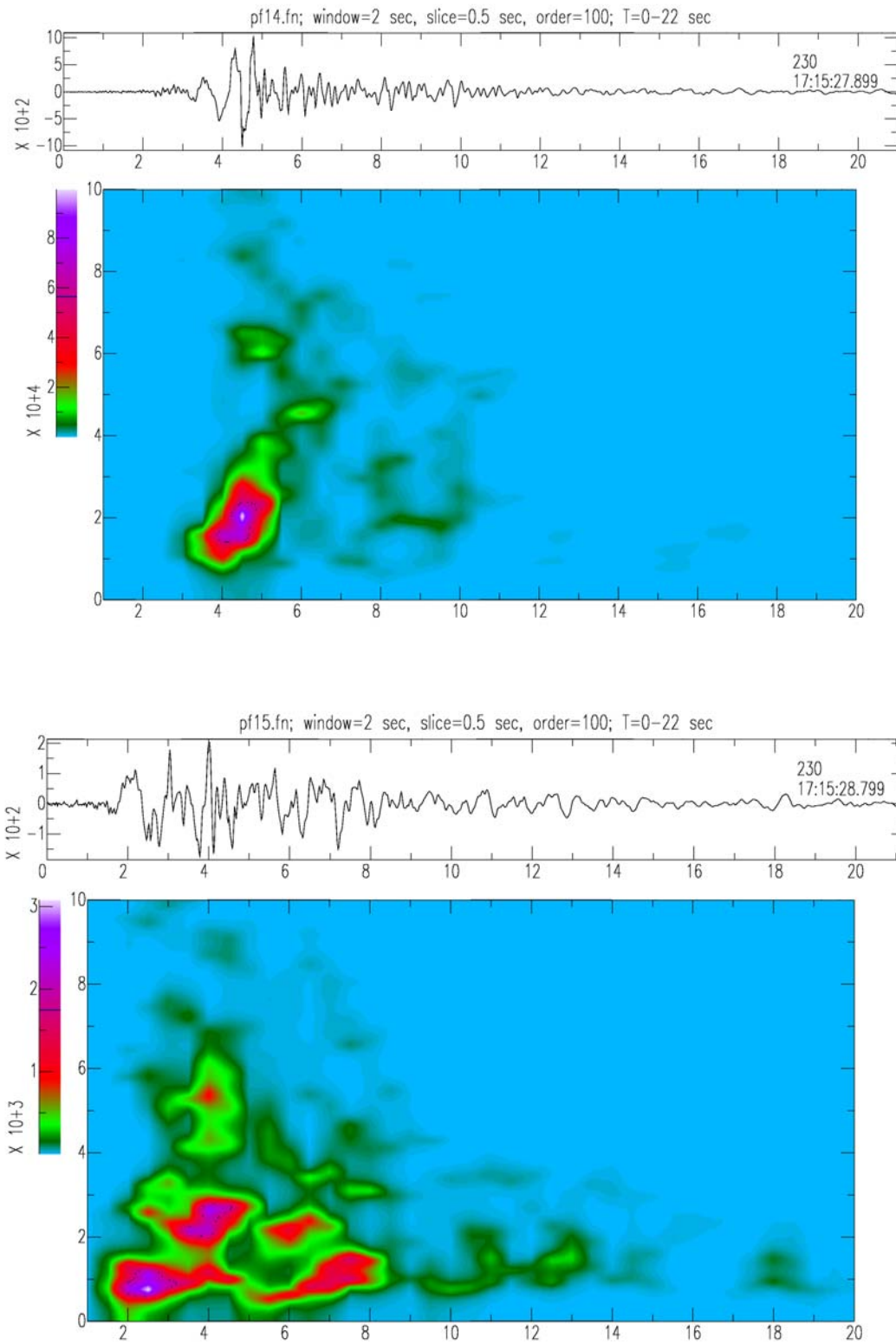


**Figure 2.** Spectrograms of recorded acceleration at stations PF14 (top panel) and PF15 (bottom panel). Acceleration unit is cm/s. Note that the peak spectral acceleration at PF14 is 30 times higher than that at PF15.

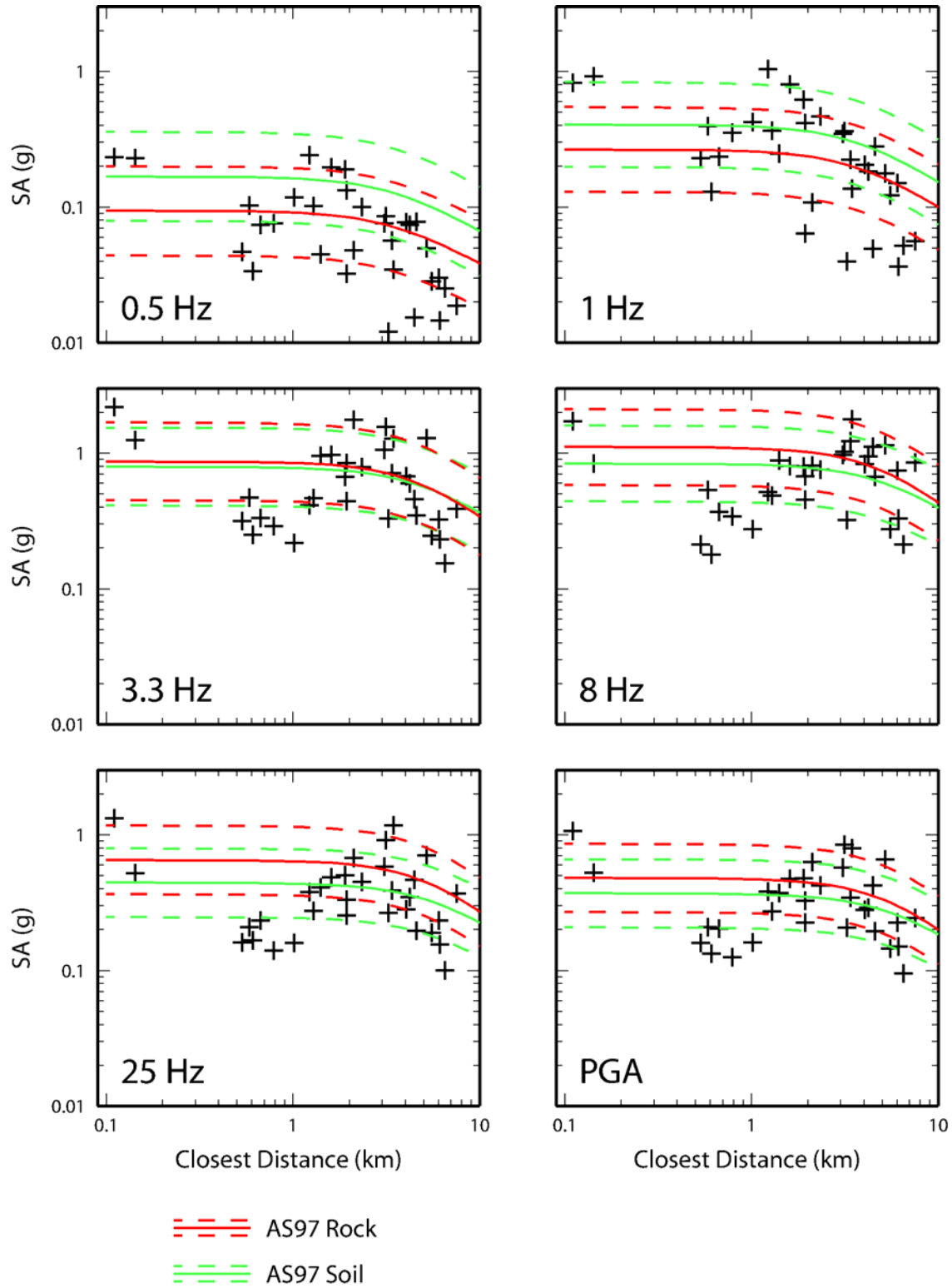


**Figure3a.** Comparison of recorded spectral acceleration (crosses) and the Abrahamson and Silva (1997) empirical attenuation model for fault normal component.

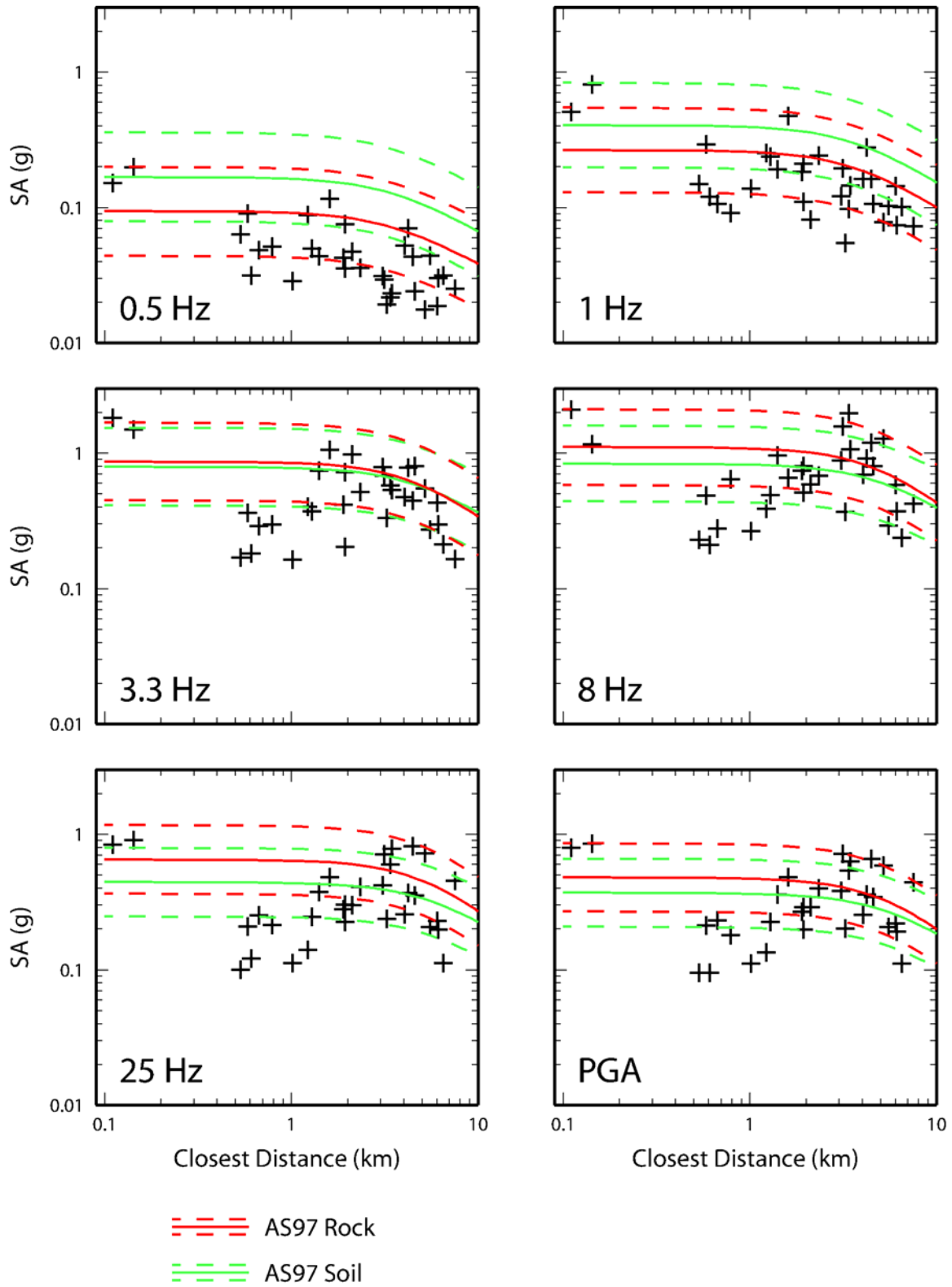


**Figure3b.** Comparison of recorded spectral acceleration (crosses) and the Abrahamson and Silva (1997) empirical attenuation model for fault parallel component.

spectrum calculated as the log average of all smoothed spectra. In order to reduce possible discrepancies due to the velocity contrast in the fault region the reference spectrum was calculated separately for stations on the east and west side of the fault. The calculated spectral ratio at a given frequency was considered as the local amplification factor.

The amplification factors estimated at frequencies 0.5Hz, 1Hz, 3Hz, 8Hz, 12Hz and 25 Hz are shown in Figure 5. In this figure closed blue circles correspond to amplitude ratios larger than 1, indicating amplification, and green circles correspond to amplitude ratios smaller than 1, indicating deamplification. A circle's radius is proportional to the corresponding amplification factor. The biggest site amplification of 3.6 is observed at 1Hz at station PF14. Our analyses indicate that site effects at this site have amplified the ground motion on a broad frequency range. Based on this result we believe that the very high acceleration observed at this station is mainly due to site effects and to a lesser extent to fault rupture effects. This is also supported by another study of local site effects at station PF14 and nearby sites (Haddadi et al., 2006). According to their investigation of ground motion acceleration record at station PF16 which was clipped during the Parkfield earthquake, the peak acceleration may have exceeded 2.5g. Also ground motion records from aftershocks of the 2004 Parkfield earthquake, 1983 M6.5 Coalinga earthquake and M6.0 San Simeon earthquake at station PF14, PF16 and their vicinity are characterized by elevated amplitudes at these particular sites. Based on waveform analyses they demonstrated that the cause of the amplification is the local site effects.

Clear trends in the amplification factors that reflect site effects are the followings:

1. The fault zone amplifies the ground motion at frequencies 1Hz and lower. The amplification is more pronounced at sites located in both ends of the fault. Note that 1Hz falls in the frequency range where also the directivity effect is expected to amplify the fault-normal component of ground motion for this type of earthquake. At most of the sites located within 1km from the fault, fault zone and site effects deamplified the ground motion acceleration, and amplified the ground motion velocity.
2. High frequency site effects are negligible at stations near the southern end of the fault where the ground motion was relatively high.

### Rupture Kinematics

#### Inversion Method

The method for determining the slip time history and slip distribution on the fault is similar to that developed by Hartzell and Heaton (1983). The fault plane is discretized into a grid of subfaults. We then impose a slip band propagating over the fault plane starting at hypocenter. The individual sets of grid points that are contained within a slip band at any time step are combined into one large set that are cast into a normal equation of the form  $Ax=b$  where  $A$  contains the Green's functions from every grid point to every station,  $x$  is the vector containing the slip value that we are trying to solve for, and  $b$  the vector containing all the data. The normal equation is solved using a least squares solver with positive constraint (we do not allow for

reverse slip). Our method allows for variable rake, in which case every original grid point is split into two grid points where the new rake angles are different from the original by  $+45^\circ$  and  $-45^\circ$  respectively, so that the same positivity constraint can be used. In order to stabilize the solution we applied spatial smoothing constraints as well as smoothing of the two perpendicular rake vectors. The smoothing and damping parameters used in solving the linear equations are determined by trial-and-error.

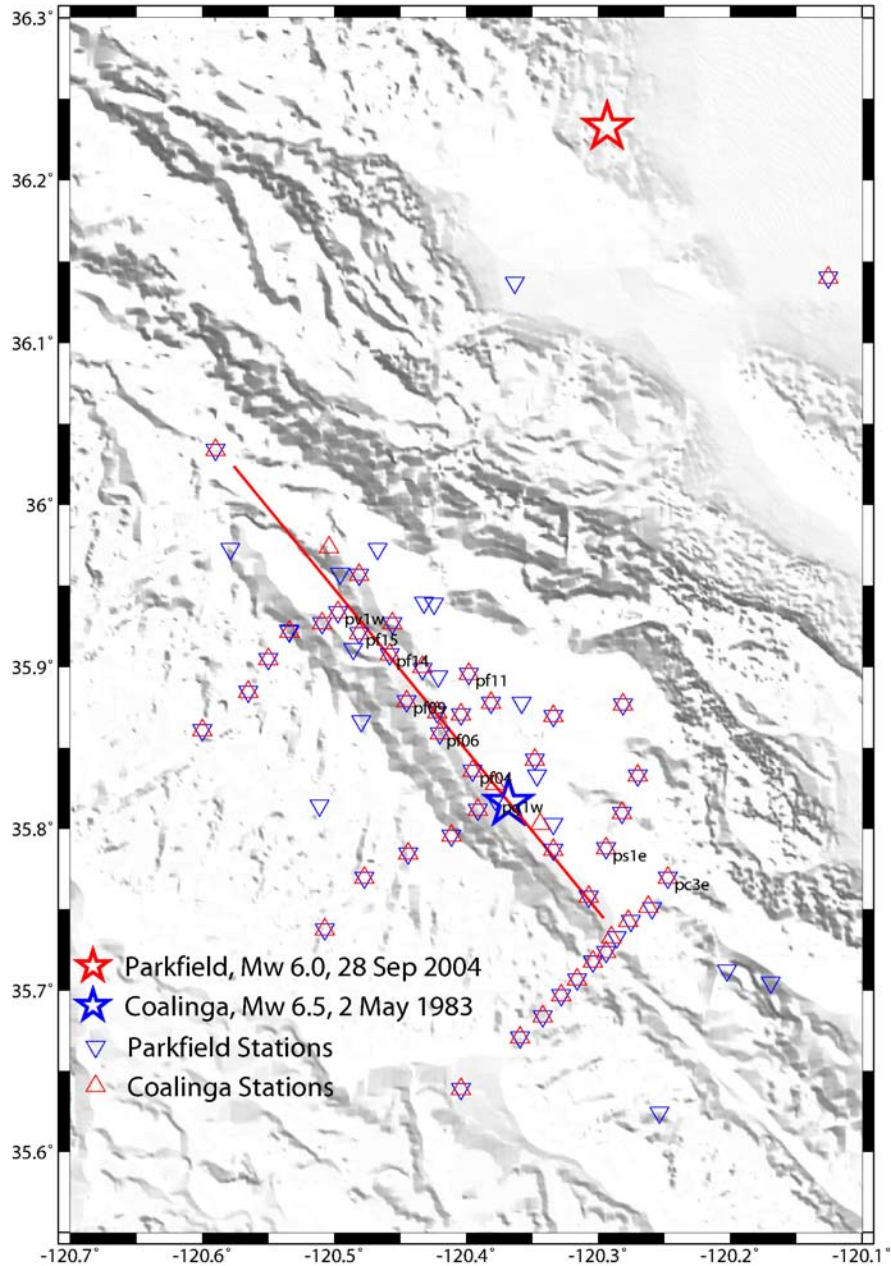


**Figure 4.** Map of the Parkfield area showing the location of the stations that recorded 2004 Parkfield earthquake (blue triangles) and Coalinga earthquake (red triangles). Also shown are the epicenter of the Parkfield earthquake (blue star) and the epicenter of the Coalinga earthquake (red star).

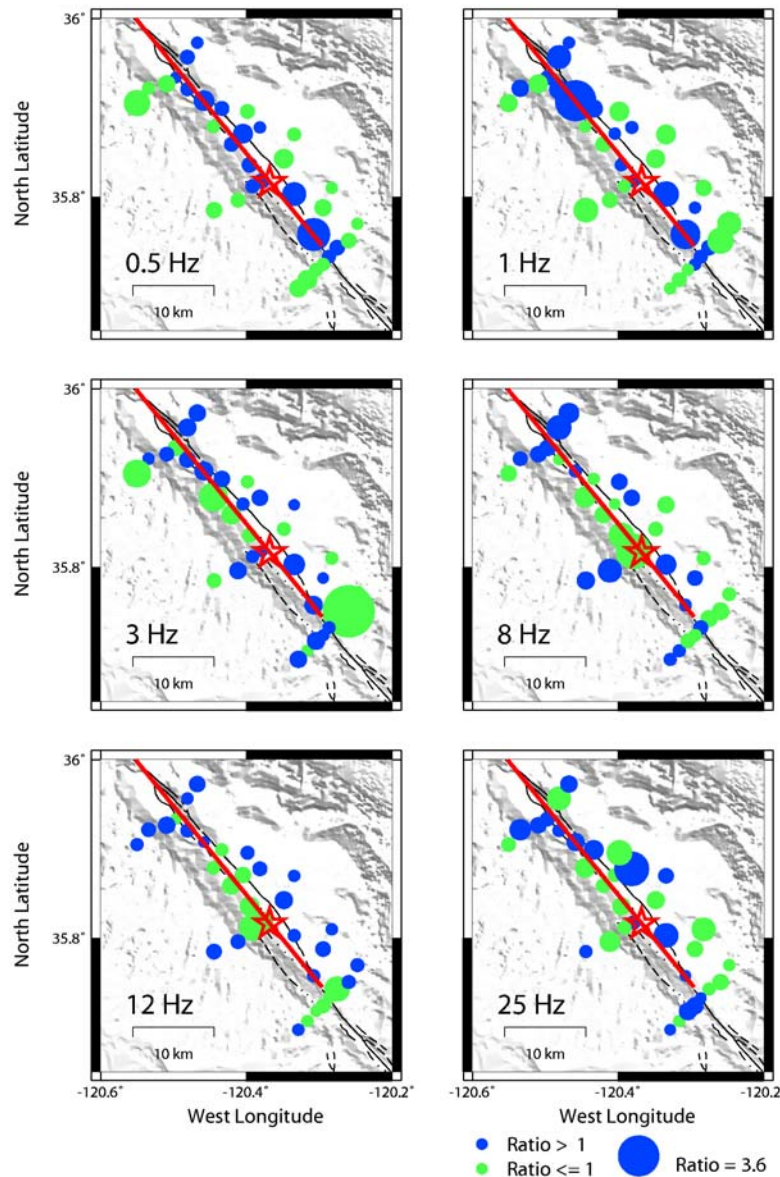


**Figure 5.** Site effect amplification factors estimated at stations that recorded the Coalinga earthquake. A circle’s radius is proportional to the amplification factor. Blue circles indicate amplification and green circles indicate deamplification. Note that the largest amplification of 3.6 was observed at 1Hz at station PF14 which also recorded the highest acceleration during the 2004 Parkfield earthquake

We set up the rupture plane as single fault plane with a strike angle of  $140.8^\circ$  and dip angle of  $89^\circ$ . The length of the fault plane is 35 km and the width 16 km. The depth to the top of the fault is 0.1 km. In our inversion we used ground motion data recorded at stations with the fault distance smaller than 30 km. We excluded most of the stations with fault distance less than

1 km. These stations were excluded from the inversion for several reasons. First, with our current representation of the fault surface by a single plane, stations that are very close to the fault may project on the wrong side of the fault plane. Second, some of these stations are affected by the 3D structural heterogeneities in the fault zone that are not presented in the 1D velocity models used in generating the Green's functions.

The original acceleration data were integrated to velocity and band-pass filtered at 0.1-1 Hz. The 1D velocity models shown in Table 1a and 1b were used to calculate Green's functions for sites located on the east and west sides of the fault, respectively. The two models differ from each other in the top 10 km, with the west side model being 20% faster in the top 10 km (e.g. Thurber et al., 2003). The west side 1D velocity model was derived from wave path calibration analyses in the region.

Since we inverted relatively high frequency ground motion velocity the 1D Green's functions were also corrected for local site effects using site-specific amplification factors. These factors were derived using the empirical relations of Borchardt (1994) and  $V_S^{30}$  value. Although very simplistic, the correction improves the quality of the slip inversion. In our trial inversions we varied the maximum rupture velocity between 2.5 and 3.5 km/s, but found that 3.0 km/s gave the best waveform fit. We used 20 time windows with duration of 0.8 sec and superposed by 0.4 sec.

**Table 1a.** 1D Velocity Model Parameters. East of the Fault

Thick.	Vp	Vs	Density	Qp	Qs
0.002	1.70	0.35	2.00	80	20
0.004	1.80	0.55	2.00	80	30
0.006	1.80	0.80	2.00	80	40
0.008	1.90	0.90	2.00	100	40
0.010	2.00	1.00	2.00	100	40
0.070	2.40	1.30	2.00	200	60
0.20	2.66	1.40	2.00	50	60
0.20	3.24	1.80	2.00	50	80
0.50	3.28	1.90	2.00	50	105
1.00	3.60	2.07	2.10	100	110
2.00	3.76	2.17	2.20	200	120
3.00	5.35	3.10	2.60	200	130
3.00	5.65	3.26	2.60	200	140
16.00	6.37	3.68	2.81	200	150
12.00	7.76	4.48	3.25	600	170
4.00	7.90	4.56	3.30	700	180
0.00	7.99	4.61	3.33	1000	200

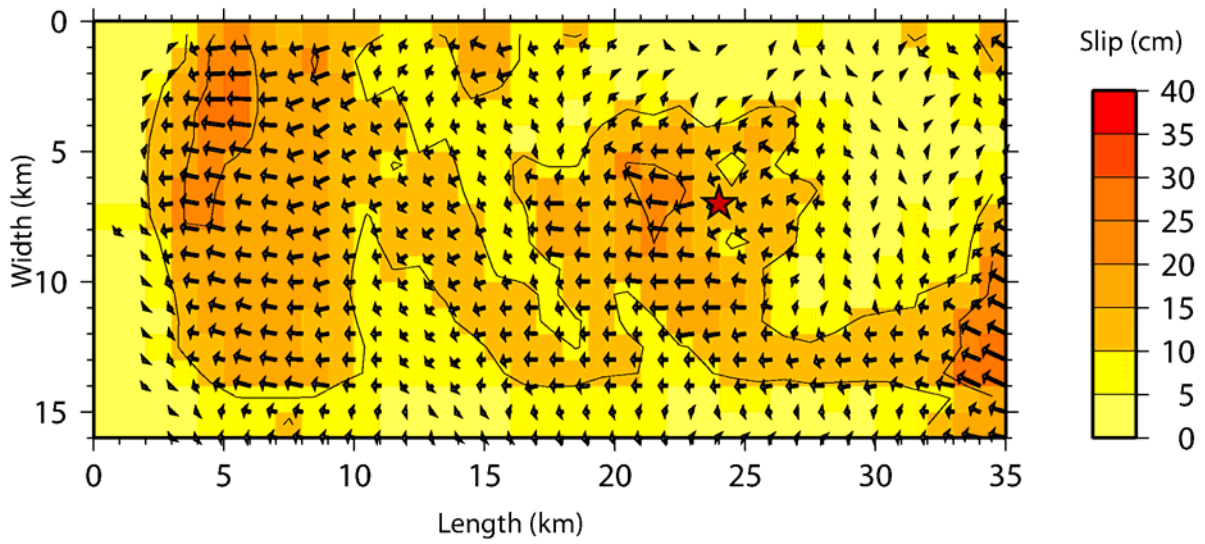
**Table 2a.** 1D Velocity Model Parameters. West of the Fault

Thick.	Vp	Vs	Density	Qp	Qs
0.002	1.70	0.35	2.00	80	20
0.004	1.80	0.55	2.00	80	30
0.006	1.80	0.80	2.00	80	40
0.008	1.90	0.90	2.00	100	40
0.010	2.00	1.00	2.00	100	40
0.070	2.40	1.30	2.00	200	60
0.20	2.80	1.50	2.00	50	60
0.20	3.60	2.00	2.00	50	80
0.50	3.86	2.23	2.01	50	100
1.00	4.23	2.44	2.12	100	110
2.00	4.71	2.72	2.28	200	120
6.00	5.95	3.44	2.67	200	130
16.00	6.37	3.68	2.81	200	150
12.00	7.76	4.48	3.25	500	170
4.00	7.90	4.56	3.30	700	180
0.00	7.99	4.61	3.33	1000	200

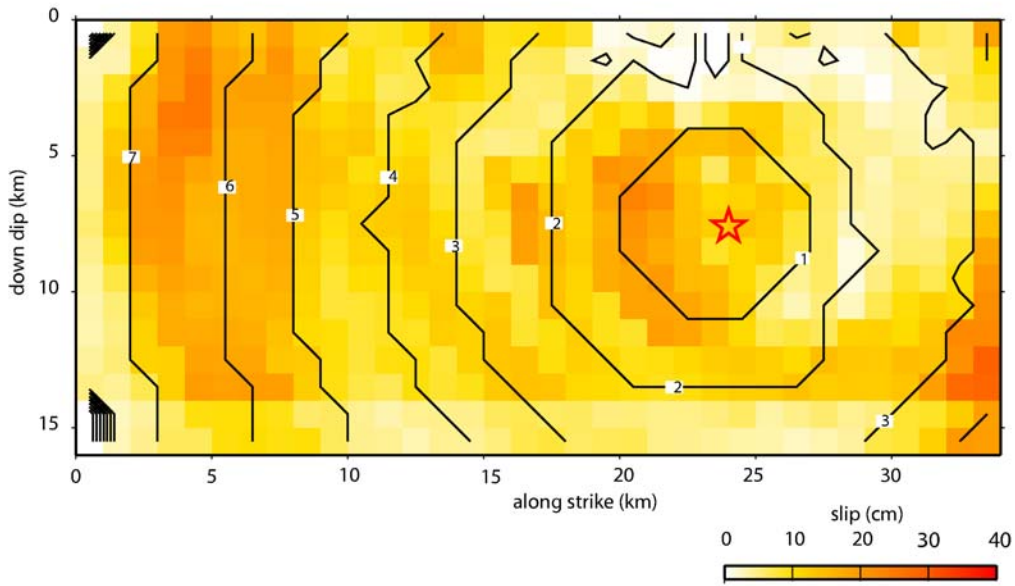
### Inverted Slip Model

Figure 6 shows the distributions of final slip, and slip vector on the fault plane. Figure 7 shows contour lines of the rupture initiation time. The waveform fits for selected stations used in the inversion is shown in Figure 8. The slip is concentrated in two large areas that occupy about 30% of the fault. The maximum slip of 40 cm is observed in a shallow slip area in the northern part of the fault. The average rake angle is 180 degrees. It indicates that this event was predominantly right-lateral strike slip. The total moment amounts to  $1.53 \times 10^{25}$  dyne.cm, corresponding to a moment magnitude of 6.1.

The only region with substantial shallow slip is in the northern part of the fault. Elsewhere the slip is relatively deep. The patch of slip located in the southern edge of the fault seems to be controlled by the large ground motion observed at nearby stations. Although not well resolved, because of its proximity to the fault boundary, the slip in the southern part of the fault indicates that the fault rupture propagated bilaterally. It quickly stopped in the southern part of the fault, probably due to a strong barrier. The ruptured fault segment is situated between a locked segment to the south and a creeping segment to the north.



**Figure 6.** Total slip and final slip vector distribution for the kinematic rupture model obtained by inverting near-fault ground motion velocity in the frequency range 0.01-1.0 Hz.



**Figure 7.** Contour lines of kinematic rupture time initiation.

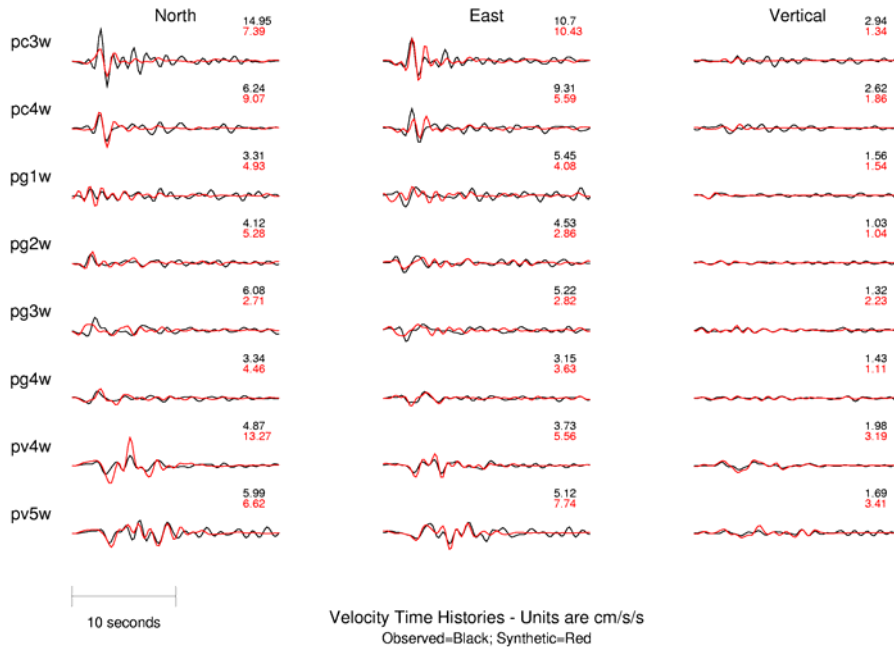
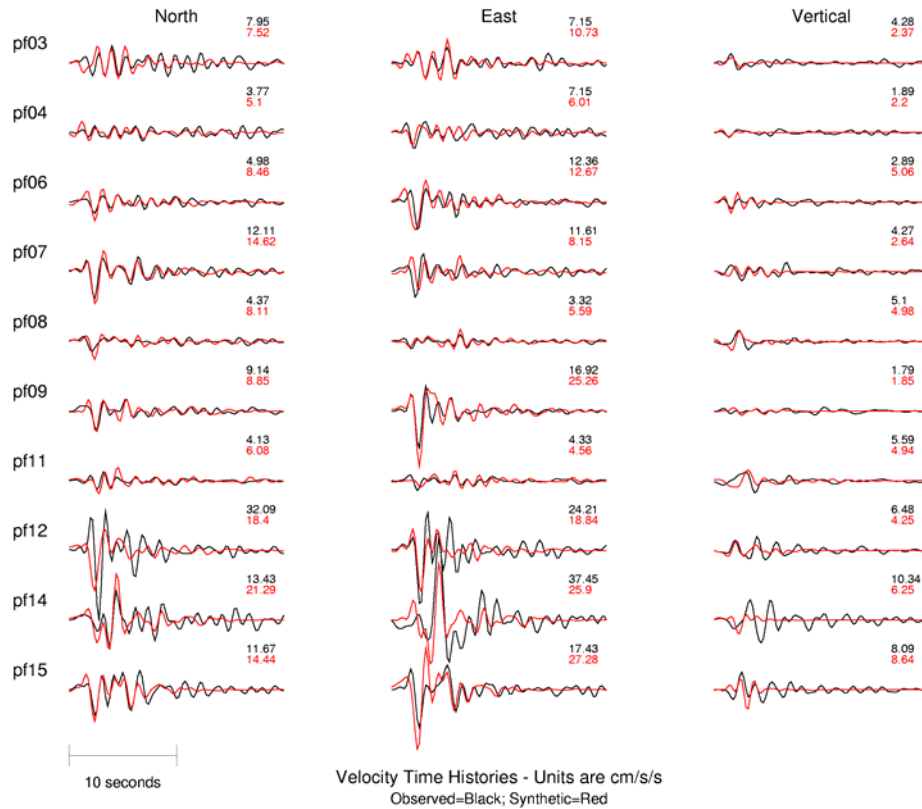


**Figure 8.** Comparison of recorded (black) and synthetic ground motion velocity (red) calculated with the kinematic model at CGS and USGS stations shown in the upper panel and lower panel, respectively.

The maximum rupture speed in our preferred model is 3.0 km/s. The kinematic rupture model indicates that the rupture speed increased as the rupture propagated away from the initiation point. The rupture gradually came to a stop in the northern end of the fault as opposed to an abrupt stop in the south where our kinematic model shows that the rupture speed was supershear for a short distance.

The shallow slip observed in the north and rupture directivity contributed to the seismic energy at frequencies above 1Hz at sites north of epicenter. We concluded that the increase in ground motion amplitude observed at stations located near the north end of the fault was caused by combined site effects and local rupture process effects. In contrast, in south at stations PS1E and PC3E neither the site effects nor rupture directivity were strong enough to be considered key factors in affecting the ground motion amplitude. In fact most of the stations in this area recorded relatively weak motion. It is possible that the larger ground motions observed at stations PS1E and PC3E were caused by the large amplitude shock wave created when the rupture in the southern part of the fault went supershear. We will elaborate more on this topic in the following section.

### **Rupture Dynamics**

#### **Inversion Technique**

Our procedure for obtaining the dynamic rupture model of the earthquake is similar to the inversion procedure proposed by Dalguer (2002). His procedure is based on a trial-and-error technique in which the spatial distributions of the dynamic rupture parameters are obtained by step-by-step modifications that improve both the waveform fit between the recorded and calculated data, and the fit between the kinematic and dynamic final slip and initial rupture time (e.g. Pitarka and Dalguer, 2003; Pitarka, 2005). In the first step of the inversion we use a kinematic rupture model to develop initial dynamic rupture parameters that are necessary for performing spontaneous rupture modeling. We start with the kinematic slip history given on a regular grid in the fault plane. The slip history is imposed as a boundary condition in a finite-difference calculation of the stress time history on the fault. The 3D finite-difference method solves the wave equation for heterogeneous media (Pitarka, 1999). The stress time history is then used to estimate dynamic rupture parameters such as dynamic stress drop, static stress drop, and strength excess. The inversion scheme starts with this initial dynamic rupture parameterization. We also assume that the spatial distribution of the slip weakening displacement is similar to that of the final kinematic slip, and its value is 25% of the kinematic final slip. The rupture modeling trials consist of executions of a 3D finite-difference computer program that models spontaneous rupture propagation. After each execution the dynamic rupture parameters are gradually modified. The first iterations are used to constrain the dynamic stress drop. The inversion procedure ends when the spatial distributions of the final slip and rupture time in the dynamic model are similar to those in the kinematic model, respectively. In the final iterations we make small modifications to slip weakening displacement  $D_c$  and strength excess aiming at further improving the fit between the synthetic and recorded ground motion velocity seismograms.

## Spontaneous Dynamic Rupture Modeling Technique

We use the staggered grid 3D-FD method with variable spacing of Pitarka and Dalguer (2003) to model wave propagation and rupture dynamics on the fault. The rupture dynamics on the fault is modeled by using the so-called the “inelastic fault zone” formulation proposed by Dalguer and Day (2004). The rupture process is controlled by a simple slip weakening law as proposed by Andrews (1976).

## Fault Parameterization

The numerical techniques for calculating stress from the slip on the fault require the time history of the slip to be smooth. This condition cannot be met by our kinematic slip model. Therefore in order to initiate the dynamic rupture inversion scheme for the Parkfield earthquake we used the kinematic model of Liu et al. (2006). In their non-linear inversion the geometry and location of the fault is similar to those used in our kinematic model. Their model was obtained by inverting the near-fault ground motion velocity, band-pass filtered at 0.1-1.0 Hz. In their technique the slip rate function is smooth. It is approximated by an appropriate combination of sine and cosine functions representing the accelerating and decelerating parts of the slip rate, respectively.

In our spontaneous rupture modeling we assumed that the fault slipped with a rake angle of 180 degrees. The FD grid spacing of 250 m used in our numerical simulation insured accurate wave propagation modeling up to 0.5 Hz. The best estimates of the final slip and initial rupture time distributions resulted from our dynamic rupture inversion are shown in Figure 9. For comparison, in this figure, we also show the targeted final slip and initial rupture time distributions from the kinematic rupture model of Liu et al. (2006). Our dynamic slip model matches well the kinematic slip model. Most importantly we succeeded to match very well details of the kinematic initial rupture time distribution, too.

## Dynamic Fault Rupture Model

The preferred dynamic fault rupture model is shown in Figure 10. The rupture parameters that we obtained through our spontaneous rupture modeling include the dynamic stress drop, static stress drop, strength excess, and slip weakening displacement.

The average stress drop is very low, less than 2 MPa. Elevated stress drops of about 5-10 MPa are concentrated in several small areas throughout the fault. Because of their relatively high stress drop, these areas of energy bursts can generate near-fault ground motion with locally large acceleration. The strength excess, which is one of the factors that controls the fracture energy, is low throughout the fault, except for the southern part where combined effects of high strength excess and low dynamic stress drop have caused the rupture to quickly stop. The rupture speed seems to have been larger than the shear-wave speed around the hypocenter and along a small portion of the southern end of the fault.

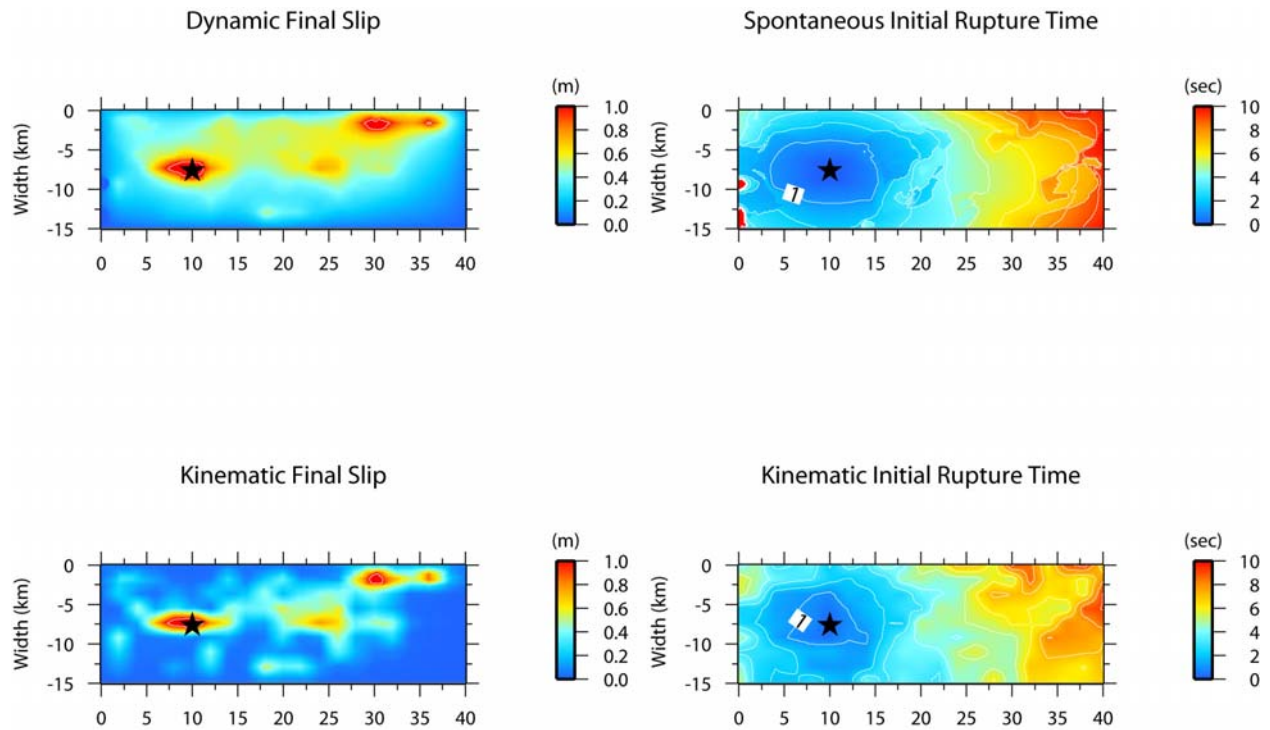


**Figure 9.** Comparison of dynamic (upper panels) and kinematic (lower panels) rupture models. Left panels show the final slip and the right panel show the initial rupture time. The kinematic model is from Liu et al. (2006).

## Discussion

The unprecedented relatively dense ground motion recordings of the 2004  $M_w$ 6 Parkfield earthquake demonstrated that near-fault ground motion of shallow strike-slip earthquakes can be extremely variable. The degree of variability for this earthquake was related more to site conditions, including fault zone effects, rather than source effects. The observation of alternated very low and very high ground motion at many sites located close to the fault, and our investigation of site effects support this conclusion.

Our study cannot give a definitive answer to the question of how much the rupture process was responsible for the localized but very high acceleration observed near the fault. Unfortunately due to the numerical requirement, our kinematic and dynamic rupture models cannot resolve the process of generation and propagation of ground motion energy at frequencies higher than 1Hz. Nevertheless there are indications that a small portion of the fault in the south ruptured with a supershear speed. As predicted by numerical and laboratory experiments this could lead to localized high acceleration at small areas offset from the fault, similar to what was observed during this earthquake. Our investigation of site effects support an important conclusion of this study that the very large ground motion at station PF14 which recorded the highest acceleration of 1.3g, was mostly due to site effects, whereas the elevated ground motion to the south of epicenter (stations PS1E and PC3E) was probably due to the shock wave generated locally as a result of the supershear rupture in that region. This is a speculation that needs further

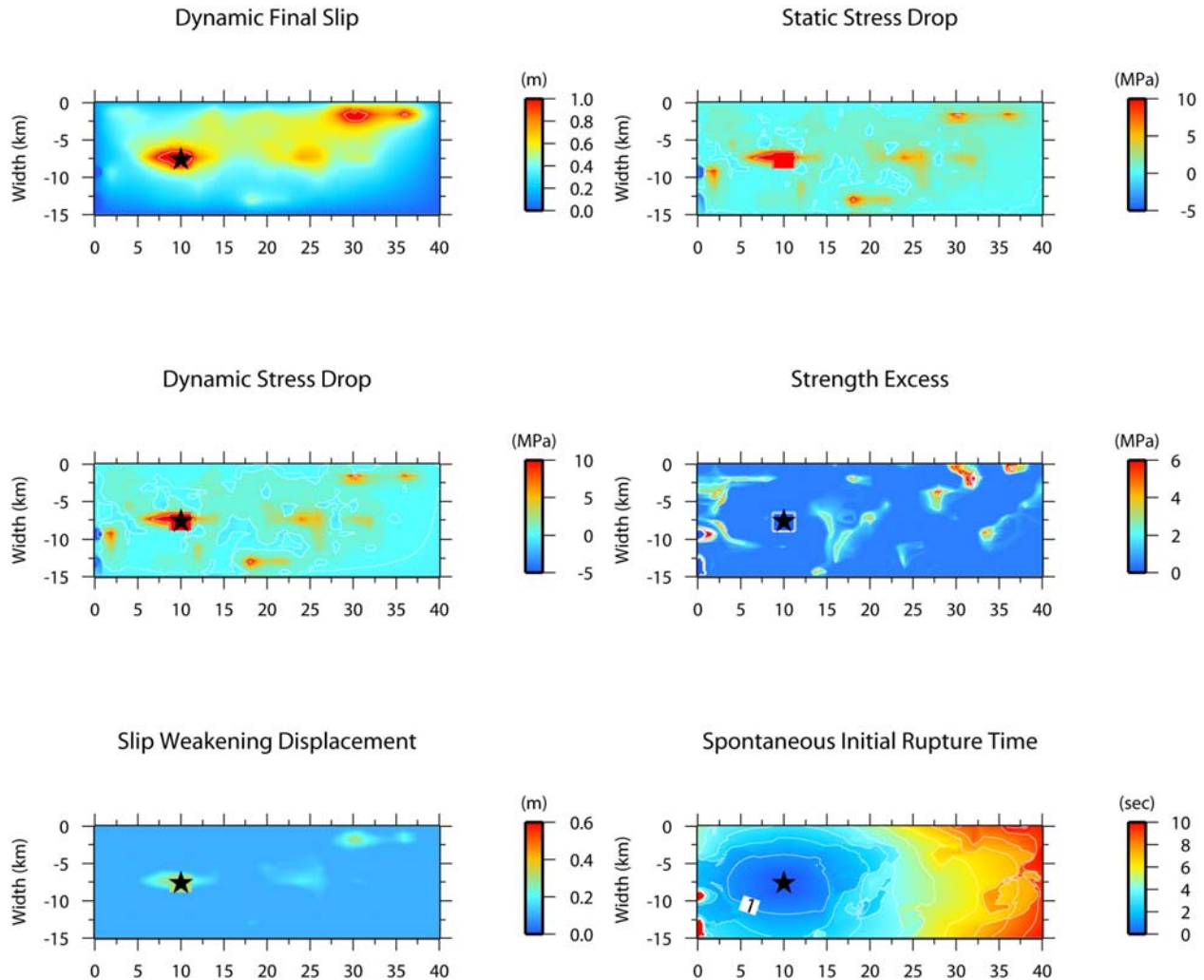


**Figure 10.** Dynamic rupture model of the 2004 Parkfield earthquake obtained by a trial-and-error inversion scheme and 3DFDM spontaneous rupture modeling. Star indicates the rupture initiation point.

investigations of the source process with higher resolution modeling and 3D wave propagation effects.

Our study leaves open the discussion about the possibility that a part of the spatial variation of high frequency ground motion was generated by very small asperities on the fault. These asperities are characterized by large stress drop and high slip velocity. These observed difference between fault-normal and fault parallel motion, which is an indication of rupture directivity effects, shows that near-fault ground motion from strike-slip earthquakes of moderate magnitude, such as the 2004 Parkfield earthquake, is affected by the rupture directivity at frequencies as high as 3 Hz.

Given the complexity in the observed ground motion and the band-limited information on the source process obtained for this earthquake it is interesting to see how well our broad-band

numerical simulation techniques perform in terms of predicting the average ground motion, the maximum ground motion and spatial variation of peak acceleration.

We simulated the recorded acceleration time history up to 10 Hz at all near-fault stations. In the simulation we used our kinematic model presented here and the technique of Graves and Pitarka (2004). The simulation technique combines deterministic and stochastic approaches to model the low frequency and high frequency parts of the acceleration time history. The simulated acceleration was finally corrected for site effects using site category and  $V_s^{30}$  values obtained from Wills et al. (2000).

Figure 11 shows the goodness of fit between the simulated and recorded ground motion. In general the spectral acceleration is matched very well at all considered periods. A negligible bias is observed. In Figure 12 we have plotted the recorded and simulated peak spectral acceleration as a function of distance at several periods, and compared it with the attenuation model of Abrahamson and Silva (1997) for this type of earthquake. The comparison shows that on average the ground motion from the Parkfield earthquake follows the existing empirical attenuation model. The simulation fails to produce the observed near-fault spatial variation of spectral acceleration. This is not surprising since, because of lack of information about the local underground structure at all strong motion sites, our simulation was mostly driven by the source process. Our study suggests that in order to capture wave propagation effects due to fault zone structure and local site conditions, 3D Green's functions and site specific corrections based on direct measurements of velocity are needed. Applying site-specific corrections, derived from the Coalinga earthquake data analyses, to the simulated peak acceleration and peak velocity results in a more favorable comparison (shown in Figure 13), especially north of epicenter.

Our main conclusion is that the relatively high and low peak acceleration, and the extremely spatially variable near-fault ground motion observed during the 2004 Parkfield earthquake were mostly driven by the local wave propagation and site effects. Unless such site effects are known, the broad-band strong motion simulation can not reproduce the ground motion variability very well. On the other hand the numerical simulation technique yields much better results than the ground motion empirical models in predicting spatial ground motion distribution and variability since it allows a better representation of the source process and underground structure characteristics.

### Acknowledgements

The authors would like to thank Anthony Shakal and Hamid Haddadi for many helpful conversations concerning this project. This research was supported by California Strong Motion Instrumentation Program.

### References

- Abrahamson, N.A. and W.J. Silva (1997). Empirical response spectral attenuation relations for shallow crustal earthquakes, *Seismological Res. Letters* **68**, 94-127.
- Andrews, D.J. (1976). Rupture velocity of plane-strain shear cracks, *J. Geoph. Res.*, **81**, 5679-5687
- Borcherdt, R. (1994). Estimates of site-dependent response spectra for design (methodology and justification). *Earthquake Spectra*, **10**(4), 617-653.

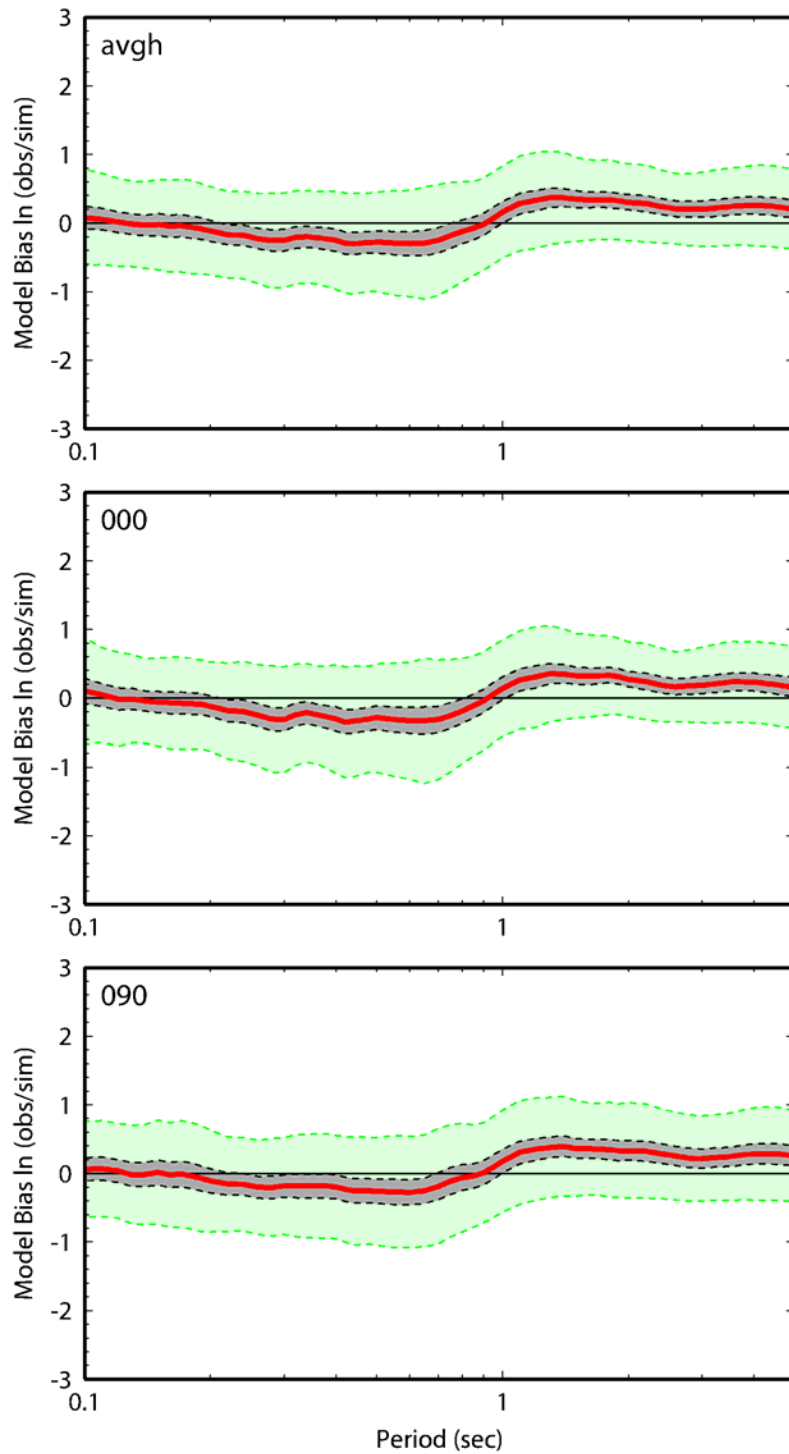


**Figure 11.** Spectral acceleration goodness-of-fit computed for the average of both horizontal components (top panel), fault parallel component (middle panel), and fault-normal component (bottom panel) for the Parkfield earthquake. Red line plots mean model bias averaged over all sites. Gray shading denotes 90% confidence interval of the mean and green shading denotes interval of one standard deviation.

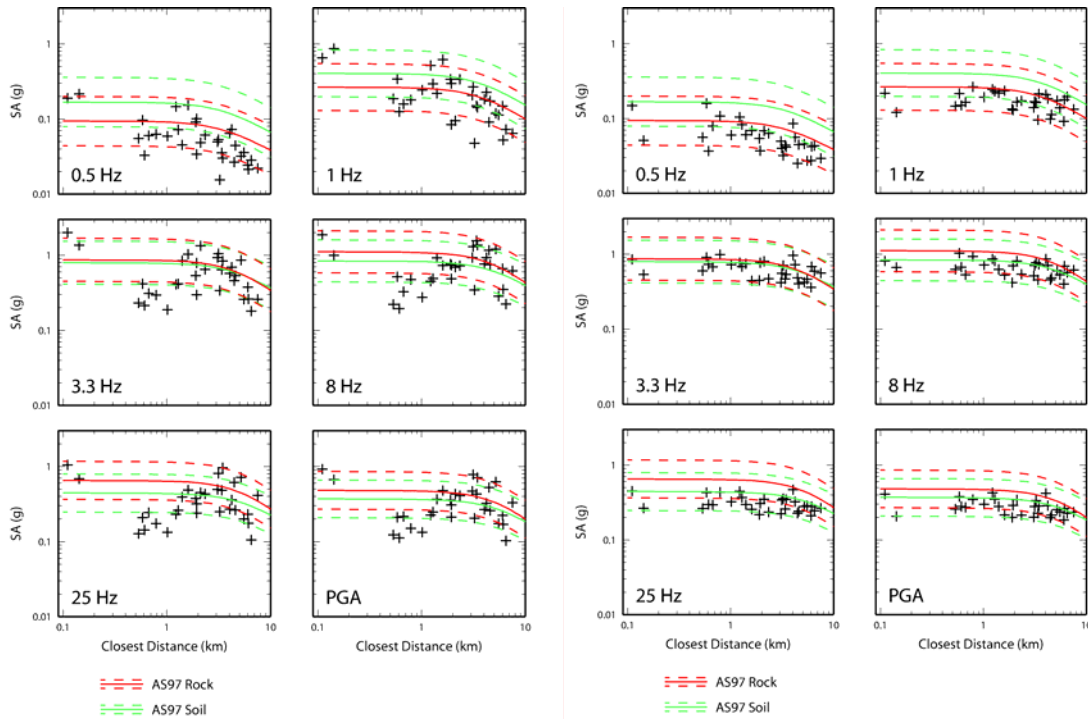


**Figure 12.** Comparison of recorded (left panels) and simulated (right panels) horizontal spectral acceleration indicated by crosses. Also shown are the Abrahamson and Silva (1997) empirical attenuation models for rock (red lines) and soil (green lines) site condition.

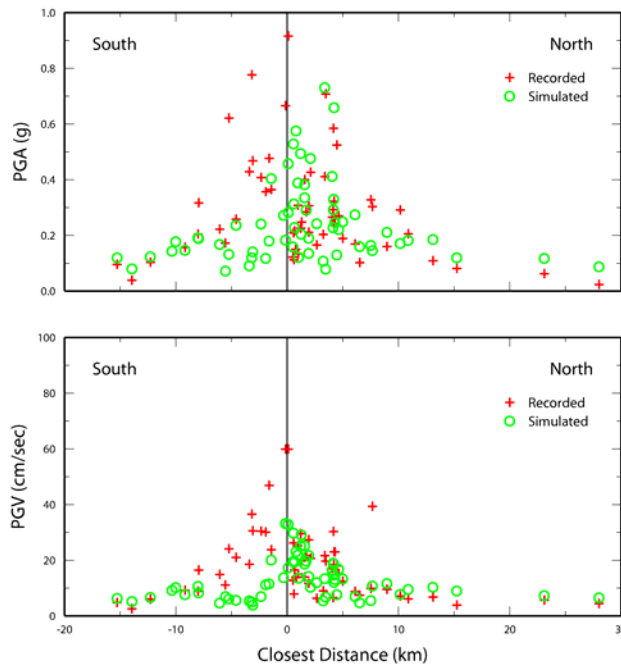


**Figure 13.** Comparison of recorded (crosses) and simulated (circles) peak ground acceleration and peak ground velocity. The simulated values include site corrections. At sites that recorded the Coalinga earthquake the site correction was derived from the analyses of weak motion data recorded during the Coalinga earthquake.

- Dickinson, W.R. (1966). Structural relations of San Andreas fault system, Cholame Valley and Castle Mountain Range, California. *Geological Society of America Bulletin*, **77**, 707-725.
- Dalguer L. (2002). Strong motion prediction based on dynamic fault modeling. 2002 Report on MEXT Project.
- Dalguer, L.A. and S.M.Day (2004) Split nodes and fault zone models for dynamic rupture simulations. EOS Trans. AGU, 85(47), Fall Meet.Supl. Abstract S41A-0944.
- Eberhart-Phillips, D. (1989). Active faulting and deformation of the Coaling anticline as interpreted from three-dimensional velocity structure and seismicity, *Journal of Geophysical Research*, **94**(13),15,565-15,586, 10.1029/89JB01390.
- Eberhart-Phillips,D., and A.J. Michael (1993). Three-dimensional velocity structure, seismicity,and fault structure in the Parkfield Region, central California, *Journal of Geophysical Research*,**98**,15,737.
- Graves, R. and A. Pitarka (2004). Broadband time history simulation using a hybrid approach. Proceedings of the 13<sup>th</sup> World Conference on Earthquake Engineering, Vancouver, Canada, August 1-6, 2004, Paper No. 1098.
- Haddadi,H.,A.Shakal,E.Kalkan,and P.Roffers (2006) On the strong ground shaking at the Fault Zone 16 and nearby ststions of Parkfield array. *Seism.Res.Lett.*,**77**,244.
- Hardebeck, J.L., and A.J. Michael (2004). Earthquake locations before and after the 2004 M6.0 Parkfield earthquake, *AGU Fall Meeting Abstracts*, 85 (47).
- Hartzell , S.H., and T.H. Heaton (1983). Inversion of strong ground motion and teleseismic wavefor data for the fault rupture history of the 1979 Imperial Valley, California earthquake. *Bull.Seism.Soc.Am.* **73**, 1553-1583.
- Langbein,J., R.Borcherdt, D.Dreger, J.Fletcher, J.L. Hardebeck, M.Hellweg, C.Ji, M.Johnston,J.R.Murray, and R.Nadeau (2005). Preliminary report on the 28 September 2004, M6.0 Parkfield, California earthquake, *Seismological Res.Lett.*, **76**,10-26.
- Liu, P., S.Custodio and R.J. Archuleta (2006). Kinematic inversion of the 2006 M<sub>w</sub>6.0 Parkfield earthquake including site effects. *Bull. Seism.Soc.Am.* (in press).
- Li,Y-G.,P.Chen, E.S. Cochran,J.E.vidale, and Th. Burdette (2006). Seismic evidence for rock damage and healing on the San Andreas fault associated with the 2004 M6 Parkfield earthquake. . *Bull. Seism.Soc.Am.* (in press).
- Pitarka, A. (1999). 3D elastic finite-difference modeling of seismic motion using staggered grids with nonuniform spacing. *Bull.Seism.Soc.Am.* **89**, 54-68.
- Pitarka A., and L. A. Dalguer (2003). Estimation of dynamic stress parameters of the 1992 Landers earthquake. *EOS Trans.AGU*, **84**(46). *Fall Meeting Supp. Abstract*. S52A-0109.
- Pitarka A. (2005) Rupture dynamics of the 1989 Loma Prieta earthquake , *Seismolocal Research Letters*, Vol 76, Nr.2., 252.
- Shakal, A., V. Graizer, M. Huang, H. Haddadi, and K. Lin (2005). Strong-motion data from the M6.0 Parkfield earthquake of September 28,2004. *Proceedings of SMIP05 Seminar on Utilization of Strong Motion Data, Los Angeles, CA*, 1-18.
- Thurber,C., S.Roecker,K.Roberts,M.Gold,L.Powell,and K.Rittger (2003). Earthquake locations and three-dimensional fault zone structure along he creeping section of the San Andreas fault near Parkfield, CA: Preparing for SAFOD. *Geophys.Res.Lett.* **3**, 1112, doi: 10.1029/2002GL016004.
- Wills,C., Petersen, M.,Brayant,W.,Reichle, M.,Saucedo, G.,Tan,S.,Taylor,G.,Treiman,J. (2000). A site condition map for California based on geology and shear-wave velocity. *Bull.Seism.Soc.Am.* **90**,6B, S187-S208.

